



## Effect of Zr on microstructure and mechanical properties of binary TiAl alloys

Rui-run CHEN, Xiao-ye ZHAO, Yong YANG, Jing-jie GUO, Hong-sheng DING, Yan-qing SU, Heng-zhi FU

School of Materials Science and Engineering, Harbin Institute of Technology, Harbin 150001, China

Received 14 July 2017; accepted 16 January 2018

**Abstract:** Ti43Al and Ti47Al alloys with different contents of zirconium were prepared by non-consumable vacuum arc melting furnace. The microstructure and mechanical properties were investigated. The results showed that Zr had no obvious effect on microstructure morphology of Ti43Al, while that of Ti47Al was modified from dendrites into equiaxed grains. The addition of Zr could refine the grains. Zr promoted the formation of  $\gamma$  phase significantly and the solubility values of Zr in  $\gamma$  phase were 12.0% and 5.0% (molar fraction) in Ti43Al and Ti47Al, respectively. Zr-rich  $\gamma$  phase mainly formed through  $\beta \rightarrow \gamma$  in Ti43Al- $x$ Zr (molar fraction, %) and  $\beta \rightarrow \alpha \rightarrow \gamma$  in Ti47Al- $x$ Zr (molar fraction, %). Fine-grain strengthening and solution strengthening were beneficial to improving the compressive strength while severe micro-segregation was detrimental to compressive properties. Large solubility of Zr was bad for ductility of alloys as well. The maximum compressive strengths of Ti43Al- $x$ Zr and Ti47Al- $x$ Zr were 1684.82 MPa ( $x=5.0\%$ ) and 2158.03 MPa ( $x=0.5\%$ ), respectively. The compressive strain fluctuated slightly in Ti43Al- $x$ Zr and reached the maximum value of 35.24% ( $x=0.5\%$ ) in Ti47Al- $x$ Zr. Both alloys showed brittle fracture.

**Key words:** TiAl binary alloy; zirconium; microstructure evolution; phase transformation; compressive properties

### 1 Introduction

TiAl-based alloys have attracted much attention as a substitute for nickel-based alloys as highly promising high temperature structural materials for their excellent low density, high specific modulus and creep resistance [1–3]. However, the disadvantages of poor room-temperature plasticity, poor processability and poor anti-oxidation above 800 °C have obstructed their development [4,5]. Attempts at improving the mechanical properties of TiAl alloys involve improving the manufacturing technique and adding alloying elements [6]. Manufacturing techniques such as hot forging, extrusion, directional solidification and rapid solidification can effectively improve the microstructure and mechanical properties of TiAl alloys [7–10]. The addition of alloying elements like Nb [11,12], Fe [13,14], Mo [15], B [6,16] and Cr [14,17] has made some achievements in improving the mechanical properties of TiAl alloys in recent years. The addition of Nb has been studied widely these years and the addition of elements (Mo, B, Y, etc) based on Nb-addition has been deeply researched by many scientists.

Adding elements with high melting point is an important way to improve the room-temperature mechanical properties and high-temperature oxidation resistance. For instance, the addition of Zr improves the ductility and toughness, and thus improves the processability of TiAl-based alloys at room temperature [18–20]. As a weak  $\beta$  stabilizer, Zr can improve the stability of  $\beta$  phase and lower the transformation temperature of  $\beta/\alpha$  transition [19]. Zr can substitute the place of Ti in crystal texture for being one family, which proves that Zr has an effect of solution strengthening on TiAl alloys [21]. The addition of Zr is beneficial to serving as potential nucleation core for  $\alpha$ (Al), which results in homogeneous microstructure and improved machinability [22]. Besides, the  $\beta$ -(Ti,Zr) phase may be formed at high temperature with an appropriate proportion of Zr, which may bring about the effects of strengthening or severe micro-segregation [23,24].

Peritectic reaction  $L+\beta \rightarrow \alpha$  [25] happens at 1491 °C with Al content between 44.8% and 49.4% (molar fraction), via which severe S-segregation may occur [26]. Based on the binary Ti–Al phase diagram in Fig. 1 [27], Ti43Al and Ti47Al were chosen to investigate the effect

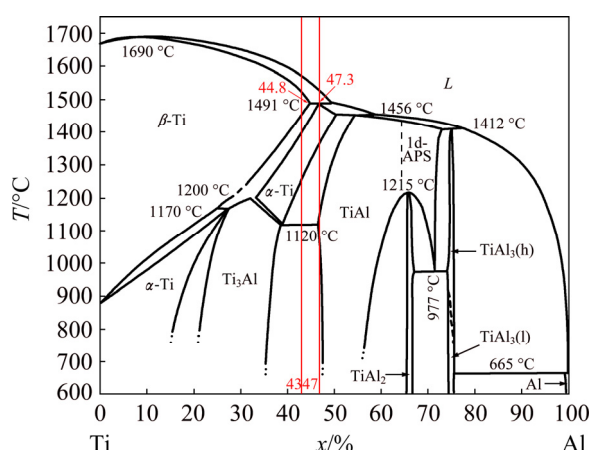


Fig. 1 Binary Ti–Al phase diagram [27]

of Zr on binary TiAl alloys. The  $\beta$  phase is the primary phase through  $L \rightarrow \beta$  with Al content lower than 49.4%. For Ti43Al, the solidification route is  $L \rightarrow L + \beta \rightarrow \beta \rightarrow \beta + \alpha \rightarrow \beta_T + \alpha \rightarrow \text{lamellar } (\alpha_2 + \gamma) + \beta_0$ . For Ti47Al, the phase transformation sequence is  $L \rightarrow L + \beta \rightarrow L + \beta + a_p \rightarrow \beta + a_p \rightarrow \beta + a_p + \alpha_s \rightarrow \text{lamellar } (\alpha_2 + \gamma) + \gamma + \beta_0$ . Here,  $\beta_T$  is the residual  $\beta$  phase,  $a_p$  is formed through peritectic reaction and  $\alpha_s$  is transformed from  $\beta$  phase. Ti43Al presents typical fully  $\beta$ -solidifying characteristic while Ti47Al alloy solidifies via peritectic reaction, which is beneficial for systematically researching the effect of Zr on binary TiAl alloys. Ti43Al– $x$ Zr ( $x=0, 1.0\%, 2.0\%, 3.0\%, 4.0\%, 5.0\%$ , molar fraction) and Ti47Al– $x$ Zr ( $x=0, 0.5\%, 1.0\%, 1.5\%, 2.0\%, 2.5\%$ , molar fraction) alloys were designed. The micro-structure evolution, solute distribution and phase constitution were investigated, the grain size and the lamellar spacing were measured, the compressive mechanical properties were tested and the fracture surface was observed. The generation mechanism of  $\gamma$  phase was further studied and the action mechanism of Zr was further analyzed.

## 2 Experimental

Alloys with nominal compositions of Ti43Al– $x$ Zr ( $x=0, 1.0\%, 2.0\%, 3.0\%, 4.0\%, 5.0\%$ , molar fraction) and Ti47Al– $x$ Zr ( $x=0, 0.5\%, 1.0\%, 1.5\%, 2.0\%, 2.5\%$ , molar fraction) were prepared by non-consumable vacuum arc melting furnace in a water-cooled copper crucible under argon atmosphere. High purity titanium sponge (99.84% purity), aluminum (99.99% purity) and zirconium (99.5% purity) were used as raw materials. Predetermined amount of each raw material was weighed with analytical balance, which was 50 g for each. The ingots were fabricated with dimensions of  $d40 \text{ mm} \times 10 \text{ mm}$ . Each ingot was melted at least five times to ensure the sufficient melting and homogenization. The mass loss was lower than 1.90% after melting.

Then, the ingots were machined in half by wire-electrode cutting. One side was machined into six columns with dimensions of  $d4 \text{ mm} \times 6 \text{ mm}$  to test the compressive mechanical properties. Another half was ground, polished and cleaned to study the phase constitution, microstructure evolution, solute distribution and micro-segregation.

The microstructure was observed by scanning electron microscope (SEM) in back-scattered electron (BSE) mode to study the microstructure evolution and micro-segregation. The phases were identified by X-ray diffraction (XRD) and energy dispersive spectrometer (EDS). The statistical volume fraction of phases was calculated by Image-Pro Plus. The room temperature compression test was carried out on an Instron–5569R testing machine with a compression velocity of 0.5 mm/min and the fracture morphology was investigated by SEM-BSE. At least five column specimens were tested for each alloy to ensure the reliable data and the average value was calculated and analyzed.

## 3 Results

### 3.1 Effect of Zr on phase constitution of binary TiAl alloys

The phase constitution of binary TiAl alloys with addition of Zr was characterized and the results are shown in Fig. 2. With the addition of Zr, the microstructure consisted of  $\gamma$  phase,  $\alpha_2$  phase and  $\beta_0$  phase for both Ti43Al and Ti47Al alloys. The diffraction peak and  $2\theta$  value remained unchanged while the diffraction peak intensity presented an apparent variation, suggesting that the phase contents varied significantly with increasing addition of Zr. According to the Bragg's equation  $2d \sin \theta = n\lambda$  ( $d$ : interplanar spacing;  $\theta$ : incident angle of X-ray beam;  $\lambda$ : X-ray wavelength) [28], interplanar spacing of the alloys expanded or shrunk with addition of Zr, implying high solid solubility of Zr in  $\alpha_2$  and  $\gamma$ . The detailed analysis of the evolution mechanism of TiAl– $x$ Zr alloys will be presented later.

### 3.2 Effect of Zr on microstructure of Ti43Al alloys

The effect of Zr on the microstructure of Ti43Al– $x$ Zr was analyzed. Figure 3 shows the microstructure characteristics and Table 1 presents the corresponding EDS results of the phases shown in the insets in Figs. 3(e) and (f). Figure 4 presents distinct element distribution of red solid line shown in the inset in Fig. 3(f). Obviously,  $(\alpha_2 + \gamma)$  lamellar structure, a small amount of  $\gamma$  phase and a tiny amount of  $\beta_0$  phase were mainly produced. The phase with offwhite contrast appeared with the addition of Zr and showed basket-weave distribution, which became compact with increasing the addition of Zr.

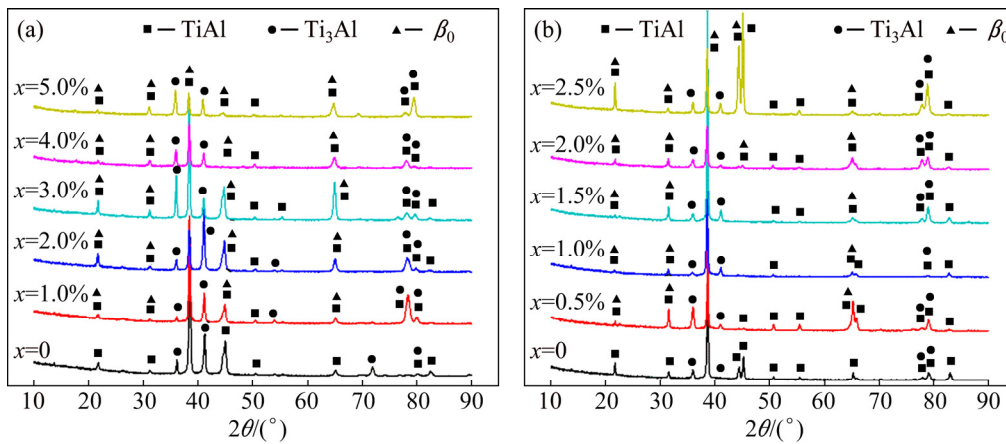


**Fig. 2** Phase constitutions of TiAl-xZr alloys with different additions of Zr: (a) Ti43Al-xZr; (b) Ti47Al-xZr

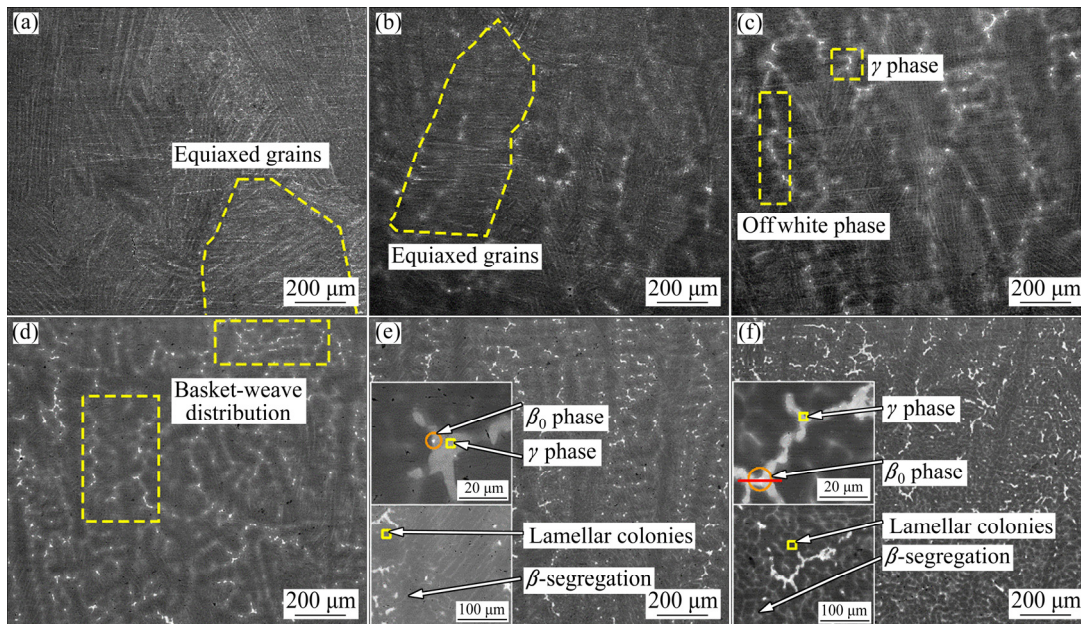


**Fig. 3** Effect of Zr content on microstructures of Ti43Al-xZr alloys: (a)  $x=0$ ; (b)  $x=1.0\%$ ; (c)  $x=2.0\%$ ; (d)  $x=3.0\%$ ; (e)  $x=4.0\%$ ; (f)  $x=5.0\%$

**Table 1** Solute distribution of insets in Figs. 3(e) and (f)

$x(\text{Zr})/\%$	Element	Molar fraction/ $\%$			
		Lamellar colony	$\gamma$ phase	$\beta_0$ phase	$\beta$ -segregation
4.0	Ti	54.02	37.12	40.4	53.93
	Al	43.2	51.23	43.59	41.32
	Zr	2.78	11.65	16.01	4.75
5.0	Ti	52.04	38.4	35.35	51.28
	Al	44.25	50.08	46.84	42.31
	Zr	3.71	11.52	17.81	6.41

In the absence of Zr, the specimen presented a typical fully lamellar microstructure with coarse lamellar colonies, as shown in Fig. 3(a). With Zr addition of 1.0%, the specimen exhibited almost fully lamellar

microstructure characteristic, and the lamellar colony was dramatically refined. The grain size (or lamellar colony size) was measured by linear intercept method and it decreased from 645.27 to 531.52  $\mu\text{m}$  (decreasing by 17.63%) with Zr addition increasing from 0 to 1.0%, indicating the effect of grain refinement. With Zr addition more than 1.0%, the lamellar colony boundaries could be hardly identified because of the increased offwhite basket-weave.

As shown in Fig. 3, small amount of offwhite basket-weave (identified as  $\beta$ -segregation according to the EDS analysis in Table 1) could be observed with addition of 1.0% Zr and it presented high contrast (identified as  $\gamma$  phase according to Table 1) at the junctions. Ti and Zr could substitute each other in TiAl binary intermediate phases largely for belonging to one family and the similar crystal structure. According to

Table 1 and Fig. 4, the content of Al in  $\gamma$  phase was about 50.0% in Ti43Al–xZr alloys, which illustrated that Zr replaced Ti and the  $\gamma$  phase could be expressed as (Ti, Zr)–Al. With increasing addition of Zr, the volume fractions of  $\gamma$  phase increased and the statistical results are displayed in Fig. 5. Strikingly, the volume fraction of  $\gamma$  phase increased from 0.31% to 3.09% with Zr addition increasing from 1.0% to 5.0%, which indicated that the addition of Zr contributed to the formation of  $\gamma$  phase. With addition of 5.0% Zr, the microstructure was the finest and most homogenous with even-distributed basket-weave, which may be beneficial to the mechanical properties.

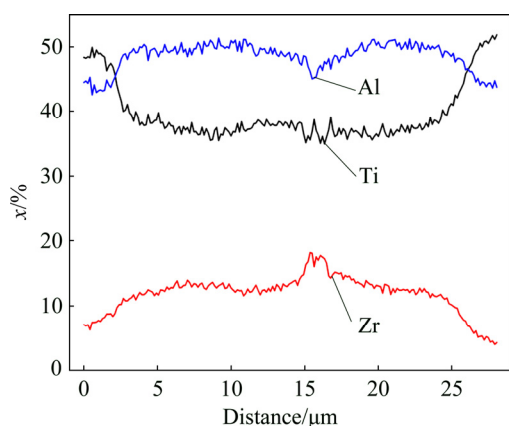


**Fig. 4** Corresponding solute distributions of inset (red solid line) in Fig. 3(f)

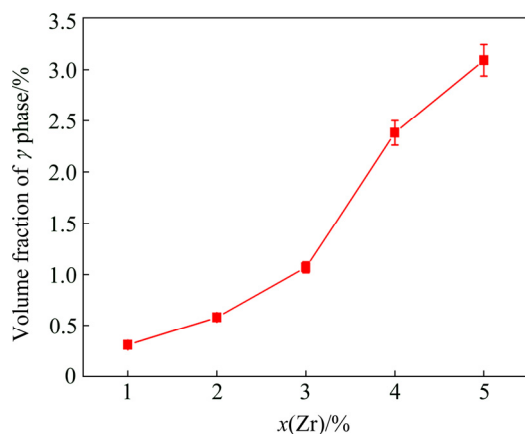


**Fig. 5** Effect of Zr content on volume fraction of  $\gamma$  phase in Ti43Al–xZr alloy

According to the EDS results at higher magnification in the insets of Figs. 3(e), (f) and Fig. 4, the contents of Zr in lamellar colonies were about 2.78% and 4.0%, which were respectively lower than the added Zr contents of 4% and 5%; while the contents of Zr in  $\gamma$  phase showed the similar contents of 11.65% and 12.0%, which were much higher than the added contents. Thus, the segregation of Zr between lamellar colonies and  $\gamma$  phase was enormous. In addition, the content of Zr in

lamellar phase increased by 43.88% while that in  $\gamma$  phase increased by 3.0%, implying that the maximum solubility of Zr in lamellar colonies did not reach, showing a value more than 4.0% and that in  $\gamma$  phase was about 12.0%. The basket-weave microstructure was rich in Zr compared with lamellar microstructure, which was supposed to be the  $\beta$ -segregation during  $\beta \rightarrow \alpha$  transition. The  $\beta_0$  phase was rich in Zr up to 16.01% and 18.0%, resulting from the insufficient decomposition of  $\beta$  phase. The high Zr-content  $\beta_0$  phase reflected large substitution of Zr for Ti at high temperature.

According to Fig. 3, several lamellar colonies showed the same orientation and they were separated by  $\gamma$  phase or  $\beta$ -segregation. The little tiny of  $\beta_0$  phase mainly existed in  $\gamma$  phase or at the boundaries of the lamellar colonies, which reflected that the  $\gamma$  phase may transfer from  $\beta$  phase directly.

### 3.3 Effect of Zr on microstructure of Ti47Al alloy

Figure 6 displays the microstructural characteristics of Ti47Al–xZr alloys with/without addition of Zr. Figure 7 shows the microstructures of Ti47Al–xZr alloys at higher magnification. Table 2 presents the corresponding EDS results of the phases shown in Figs. 7(c)–(f). All the specimens displayed a three-phase structure similar to Ti43Al–xZr alloys: lamellar colony ( $\alpha_2 + \gamma$ ),  $\gamma$  phase and  $\beta_0$  phase.

As shown in Fig. 6, the microstructure morphology showed coarse dendrites without Zr. Likewise, the specimens still presented dendrite characteristics with Zr addition of 0.5%, which was homogeneous and fine. With increasing addition of Zr, the volume fractions of  $\gamma$  phase and  $\beta_0$  phase increased, which caused the second dendrite arms (SDAS) dividing from primary dendrite arms (PDAS). Meanwhile, the  $\gamma$  phase began to interconnect like a state of network with points or strips of  $\beta_0$  phase in it. With Zr addition of 1.0% and 1.5%, the microstructure presented a mixture of dendrites and isometric dendrites (or equiaxed grains). With Zr addition of 2.0% and 2.5%, the SDAS almost disappeared and the morphology was modified into coarse equiaxed grains surrounded by gray phase.

The cubic  $\beta$  phase was found to be the primary phase by noting that the SDAS was orthogonal to the PDAS in Figs. 6(a) and (b), which exhibited a typical  $\beta$ -solidification characteristic. With increasing addition of Zr, the volume fractions of  $\gamma$  and  $\beta_0$  phases increased and the dendrites became interconnected, leading to a blurry characteristic of dendrites in Figs. 6(c)–(f). However, the morphology of dendrite characteristics could also be identified through further observation of isolated dendrites, through the solid lines shown in the insets of Figs. 6(c)–(f). In summary, Ti47Al–xZr alloys presented  $\beta$ -solidification through analysis.

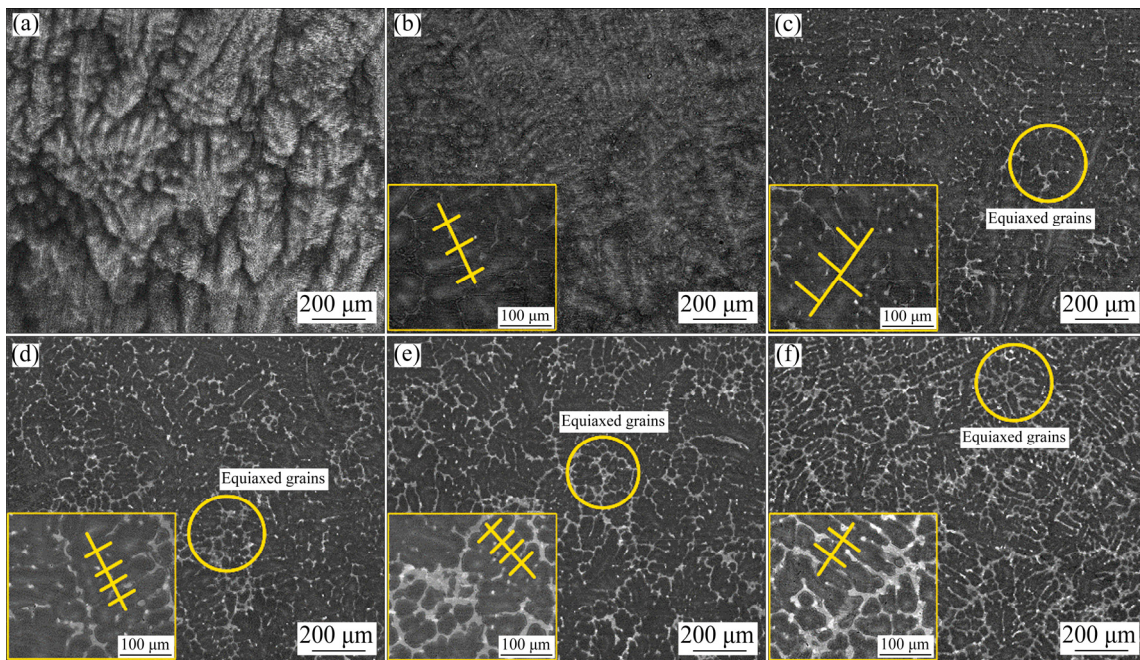


**Fig. 6** Effect of Zr content on microstructures of Ti47Al- $x$ Zr alloy: (a)  $x=0$ ; (b)  $x=0.5\%$ ; (c)  $x=1.0\%$ ; (d)  $x=1.5\%$ ; (e)  $x=2.0\%$ ; (f)  $x=2.5\%$

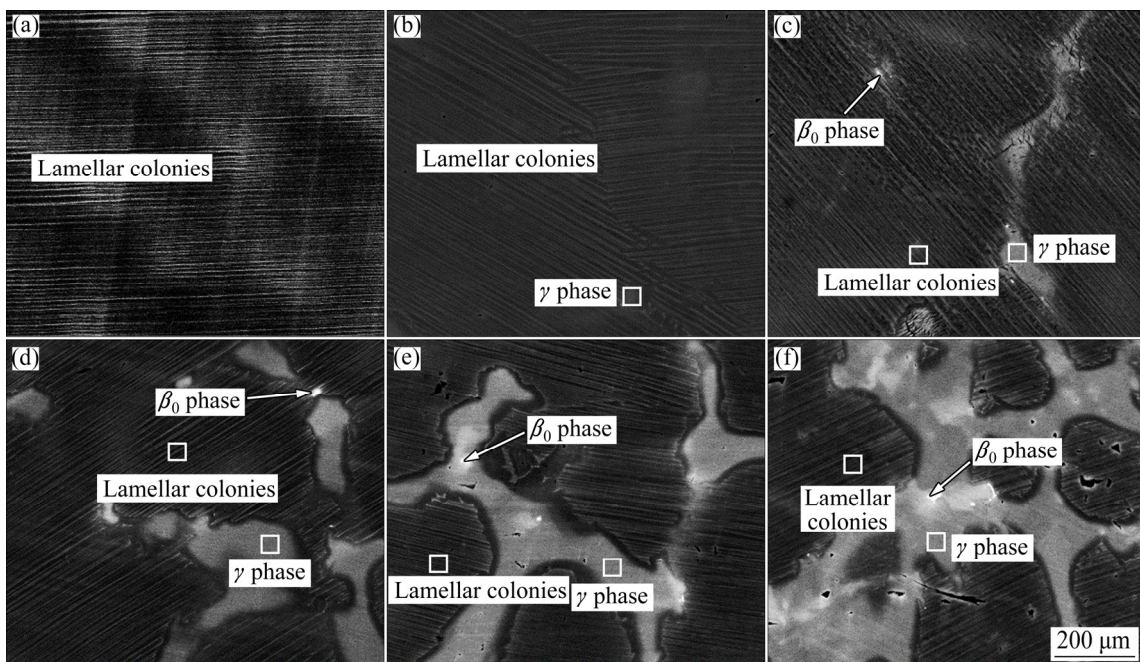


**Fig. 7** Magnified microstructures of Ti47Al- $x$ Zr alloys: (a)  $x=0$ ; (b)  $x=0.5\%$ ; (c)  $x=1.0\%$ ; (d)  $x=1.5\%$ ; (e)  $x=2.0\%$ ; (f)  $x=2.5\%$

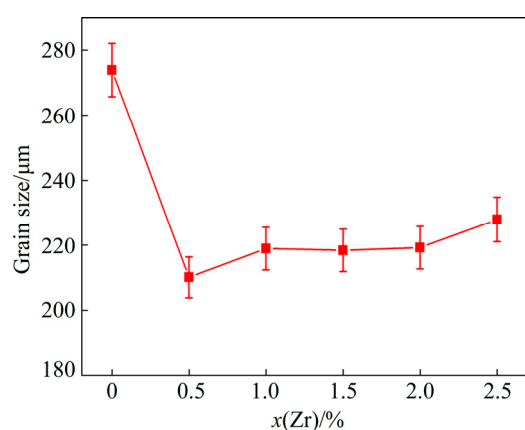
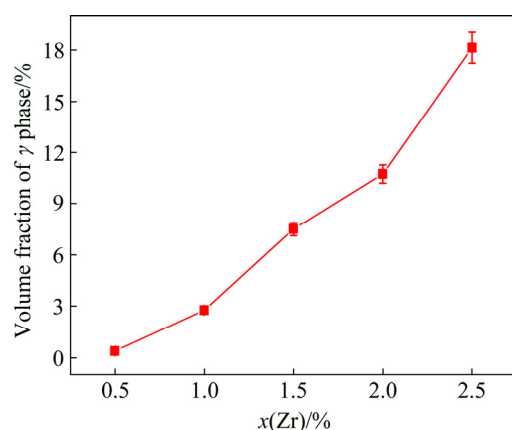
To investigate the effect of Zr on the microstructure of Ti47Al- $x$ Zr, the variation of PDAS spacing (grain size) was statistically analyzed and displayed in Fig. 8. As shown, the PDAS spacing (grain size) was 210.2  $\mu\text{m}$  with addition of 0.5% Zr, decreasing by 23.27% compared with the specimen without Zr, and kept relatively constant with Zr addition of 1.0%–2.5% (with a slight increase).

The Al-rich  $\gamma$  phase resulted from the  $S$ -segregation during solidification. Similar to Ti43Al- $x$ Zr, the  $\gamma$  phase

could be expressed as (Ti, Zr)-Al as the content of Al (about 52%) was nearly the same as the summation of Ti and Zr. It was noted that the volume fraction of  $\gamma$  phase kept increasing with increasing addition of Zr and the results of calculation are presented in Fig. 9. As shown, the volume fractions of  $\gamma$  phase increased sharply from 0.39% to 18.15% with Zr addition increasing from 0.5% to 2.5%, respectively. Similar to Ti43Al- $x$ Zr, the addition of Zr contributed to the formation of  $\gamma$  phase in Ti47Al- $x$ Zr.

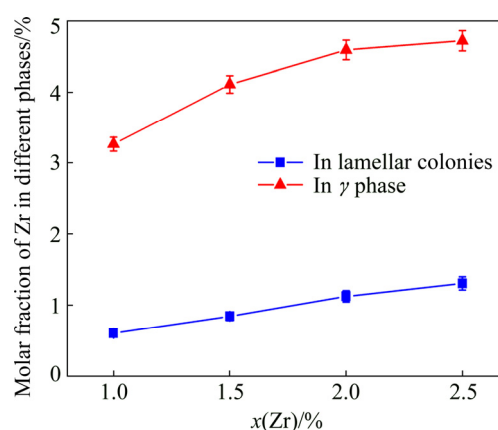
**Table 2** Corresponding solute distributions of Ti47Al–xZr (Figs. 7(c)–(f))

$x(\text{Zr})/\%$	Element	Molar fraction/%		
		Lamellar colony	$\gamma$ phase	$\beta_0$ phase
1.0	Ti	53.28	44.53	49.69
	Al	46.11	52.20	44.99
	Zr	0.61	3.27	5.31
1.5	Ti	52.21	42.94	48.37
	Al	46.94	52.94	46.97
	Zr	0.85	4.11	4.66
2.0	Ti	51.97	42.92	42.77
	Al	46.89	52.49	49.69
	Zr	1.13	4.59	7.53
2.5	Ti	51.98	43.08	46.75
	Al	46.71	52.20	44.01
	Zr	1.31	4.72	9.24

**Fig. 8** Effect of Zr content on grain size of Ti47Al–xZr alloy**Fig. 9** Effect of Zr content on volume fraction of  $\gamma$  phase in Ti47Al–xZr alloy

The difference of Zr content in lamellar colonies and  $\gamma$  phases is shown in Fig. 10. As shown, the contents of Zr in lamellar colonies were below the added values and the contents of Zr in  $\gamma$  phase were much higher,

which indicated great Zr-segregation between lamellar colonies and  $\gamma$  phase. The solid solubilities of Zr in  $\gamma$  phase and lamellar colonies were about 5.0% and 1.3%, respectively, according to Fig. 10. The bright-white  $\beta_0$  phase was observed in both lamellar colonies and  $\gamma$  phase (shown in Fig. 6 and Fig. 7) and Zr content in  $\beta_0$  phase increased to high amplitude (5.31%, 4.66%, 7.53% and 9.24%, respectively, Table 2).

**Fig. 10** Molar fractions of Zr in lamellar colonies and  $\gamma$  phase with different additions of Zr in Ti47Al–xZr alloys

### 3.4 Effect of Zr on mechanical properties of binary TiAl alloys

As discussed above, the addition of Zr could refine the grain size and modify the morphology prominently, which had decisive effect on the mechanical properties. To estimate the influence of Zr on TiAl alloys, the compression properties were tested and the results are shown in Fig. 11. In the absence of Zr, the ultimate compressive strengths were 927.21 and 1971.50 MPa for Ti43Al and Ti47Al alloys, respectively. With addition of Zr, the ultimate compressive strength and compressive strain were both improved.

For Ti43Al–xZr alloy, the compressive strength kept rising with increasing addition of Zr and it increased up to 1684.82 MPa with Zr addition of 5.0%, which was improved by 81.71%. While, the compressive breaking strain changed slightly, which fluctuated without a rule. The maximum compressive strain was 11.36% with Zr addition of 5.0%, improved by 22.28%.

In comparison, Zr could enhance the compressive strength and compressive strain with appropriate addition of Zr in Ti47Al–xZr. With Zr addition of 0.5%, the alloy presented the maximum compressive strength of 2158.03 MPa and the maximum compressive strain of 35.24%, which were improved by 9.46% and 7.64%, respectively. However, the compressive strength and compressive strain both decreased with addition of Zr more than 0.5%. It was observed that the Ti47Al–xZr alloys showed a higher ultimate compressive strength and compressive breaking strain than Ti43Al–xZr alloys.

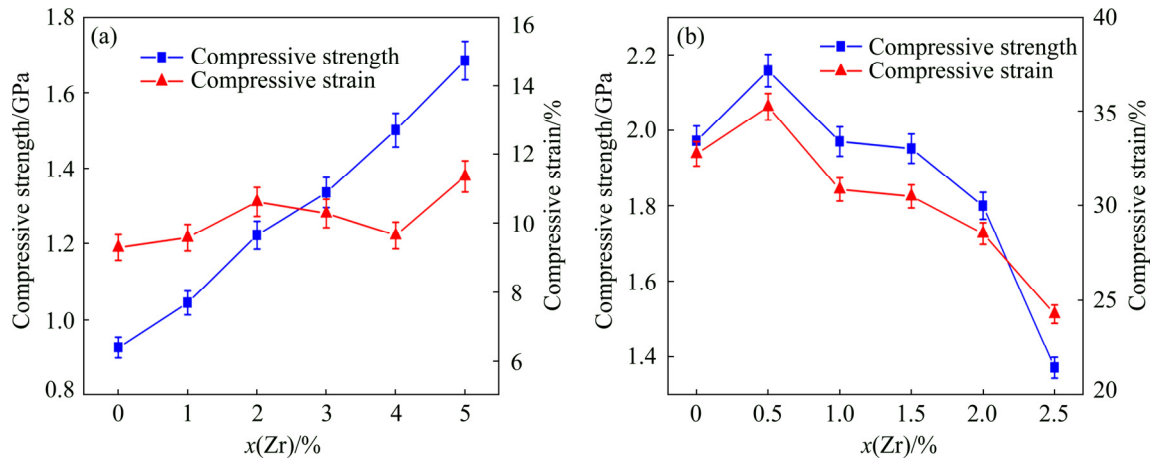


**Fig. 11** Ultimate compressive strength and compressive strain of different alloys: (a) Ti43Al-xZr; (b) Ti47Al-xZr

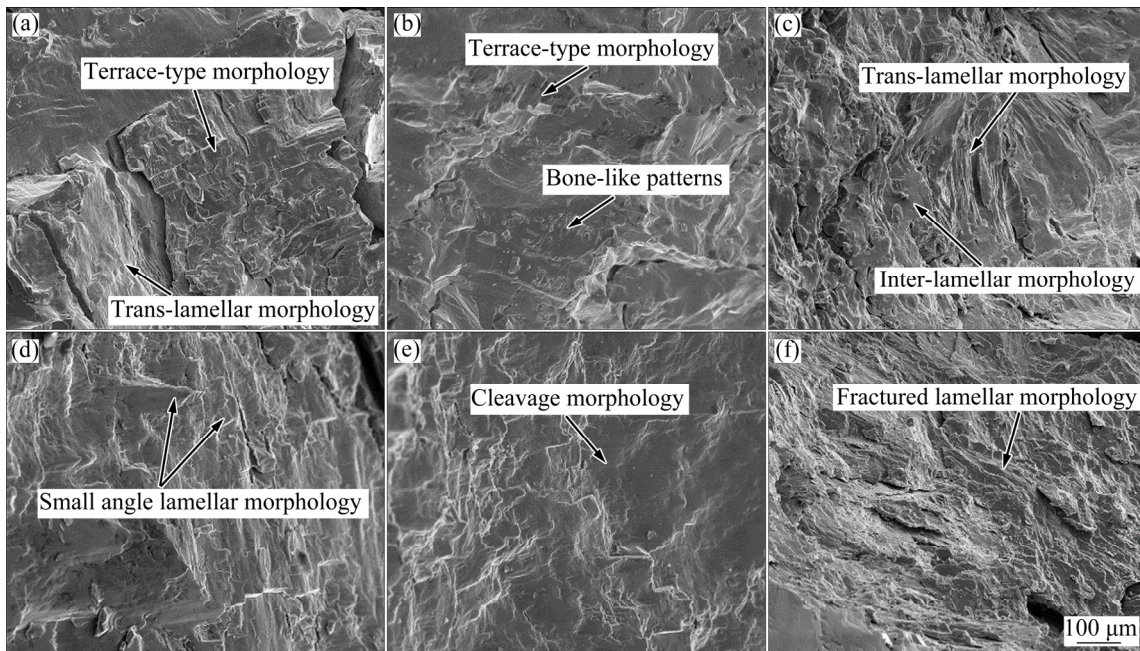


**Fig. 12** Fracture morphologies of Ti43Al-xZr (a-c) and Ti47Al-xZr (d-f) alloys: (a)  $x=0$ ; (b)  $x=3.0\%$ ; (c)  $x=5.0\%$ ; (d)  $x=0$ ; (e)  $x=0.5\%$ ; (f)  $x=2.5\%$

Figure 12 shows typical BSE fracture morphologies of Ti43Al-xZr ( $x=0$ , 3.0% and 5.0%) and Ti47Al-xZr ( $x=0$ , 0.5% and 2.5%). Obvious terrace-type morphology is presented in Fig. 12(a), and the line in the trans-lamellar fracture may be led by twin crystal or dislocation glide. The bone-like patterns and terrace-type morphology are shown in Fig. 12(b). In Fig. 12(c), clear evidences such as inter-lamellar (fracture parallel to lamellar, cleavage surfaces) and trans-lamellar (fracture across lamellar) morphologies could be observed. Trans-lamellar and inter-lamellar fractures are the dominating modes due to the higher percentage of small angle lamellar structure in Fig. 12(d), which presents brittle fracture. Fractured lamellar mode could also be observed in Fig. 12(f). However, less characteristics of brittle fracture are observed in Fig. 12(e), suggesting better

ductility with addition of 0.5% Zr in Ti47Al-xZr alloy. In conclusion, the fracture morphology mainly consisted of cleavage facets exhibiting a terrace-type morphology, river-markings and fractured lamellar mode, implying that Ti43Al-xZr and Ti47Al-xZr showed brittle fracture.

## 4 Discussion

Based on the experimental results above, Zr had significant influence on the microstructure, solute distribution, phase constitution and mechanical property of Ti43Al and Ti47Al alloys. With addition of Zr, the microstructure was well modified with fine grains and Zr-rich  $\gamma$  phase formed; the compressive strength was optimized with a great improvement and the compressive strain was improved.

#### 4.1 Phase transformation

As mentioned in Sections 2.2 and 2.3, the coarse and inhomogeneous microstructures of Ti43Al and Ti47Al were both transformed into fine and homogenous microstructures with addition of Zr, though the evolution process was different. By comparison, Ti43Al-xZr presented relatively homogenous microstructure, while Ti47Al-xZr showed microstructure with severe S-segregation.

For Ti43Al-xZr alloys, the  $\beta$  crystal was the primary phase and the microstructure showed non-dendrite columnar crystals without peritectic reaction, which belonged to full  $\beta$ -solidification. The morphology showed no obvious change with addition of Zr; whereas for Ti47Al-xZr ( $x=0$  and 0.5%),  $\alpha_p$  was produced because of peritectic reaction and the  $\beta$  grain was transformed to dendrites, which belonged to the  $\beta$ -solidification via peritectic reaction. With increasing addition of Zr, the SDAS was divided from the PDAS by  $\gamma$  phase, causing the microstructure varying from dendrites to isolated dendrites or equiaxed grains.

For Ti43Al-xZr alloys (as shown in the insets of Fig. 3), the  $\gamma$  bands were frequently observed at the location of  $\beta$ -segregation and the  $\beta_0$  phase mainly existed in  $\gamma$  phase, which suggested that the  $\gamma$  phase was transformed from  $\beta$  phase by solid-state transformation during cooling [29,30]. CHENG and LORETTO [31] introduced two ways of the decomposition of  $\beta$  to  $\gamma$  phase: by direct nucleation at high temperature or by discontinuous coarsening at lower temperature. The latter was much easier by the discontinuous coarsening of  $\gamma$  lamellae. Here, the transition may mainly be the direct nucleation because the  $\gamma$  phase showed no obvious

location along  $\gamma$  lamellae. The  $\beta \rightarrow \gamma$  transition through rapid solidification was also certificated in the study of TETSUI et al [32]. As a  $\gamma$ -stabilizer and a  $\beta$ -stabilizer, Zr could expand the  $\beta$  phase region and shrink the  $\alpha$  phase region by decreasing the temperature of  $\beta \rightarrow \alpha$  transition and raising the temperature of  $\alpha \rightarrow \gamma$  transition [32], which contributed to the  $\beta \rightarrow \gamma$  transition. The actual solidification process of Ti43Al-xZr alloys was  $L \rightarrow L+\beta \rightarrow \beta \rightarrow \beta_1+\alpha+\gamma \rightarrow$  lamellar colonies ( $\alpha_2+\gamma$ )+ $\gamma+\beta_0$  and the schematic of solidification process is presented in Fig. 13(a).

For Ti47Al-xZr alloys, the  $\beta_0$  phase existed in both lamellar colonies and  $\gamma$  phase, and the  $\gamma$  bands appeared in lamellar colonies. Additionally, with nominal composition of 47.0% Al (molar fraction) near peritectic point (47.3% Al), large amount of peritectic reaction occurred. The  $\gamma$  phase should be transformed from  $\alpha$  phase. With rapid solidification, peritectic reaction  $L+\beta \rightarrow \alpha$  insufficiently proceeded with  $\beta$  phase (BCC) remaining. Then, some  $\alpha$  phase turned into  $\gamma$  phase and the other  $\alpha$  phase turned into lamellar structure ( $\alpha_2+\gamma$ ). The remained  $\beta_0$  phase obtained from  $\beta$  (Ti,Zr) was rich in Ti and Zr. The  $\gamma$  phase obtained from  $L \rightarrow \beta \rightarrow \alpha \rightarrow \gamma$  was rich in Zr, resulting from the preferential concentration of Zr in  $\gamma$  phase. Figure 13(b) shows the schematic diagram of solidification of Ti47Al-xZr alloys.

It was also noteworthy in Fig. 3 and Fig. 7 that the adjacent lamellar colonies separated by  $\gamma$  bands or Zr-rich basket-weave often had the same orientation. Therefore, it presented large regions with uniform alignment lamellae. As mentioned research in Ref. [33], if lamellar colonies came from the  $\alpha$  grains within a same parent  $\beta$  grain, the distribution of lamellar interface traces was not random, as shown in Fig. 13.

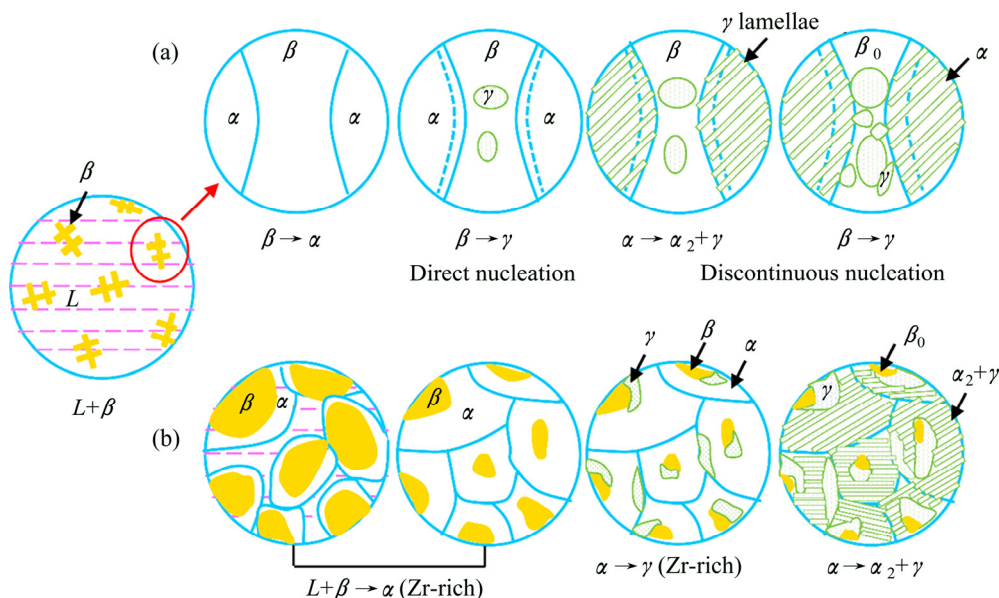


Fig. 13 Schematic diagrams of solidification process: (a) Ti43Al-xZr; (b) Ti47Al-xZr

## 4.2 Action mechanisms of Zr

As mentioned in Sections 2.2 and 2.3, the contents of Zr in  $\gamma$  phase were much higher than those in lamellar colonies (shown in Table 1 and Fig. 10), indicating that Zr preferred to concentrating in  $\gamma$  phase rather than in lamellar colonies and Zr was a  $\gamma$ -stabilizer. In Ti43Al-xZr alloys, the  $\beta$ -segregation was rich in Zr compared with lamellar colonies, which suggested that Zr preferred to concentrating in  $\beta$  phase rather than in  $\alpha$  phase or partitioning coefficient  $k(\alpha/\beta)$  ( $k(i/j)=x_i/x_j$ ,  $x_i$  and  $x_j$  are the equilibrium mole fractions of Zr in phases at equilibrium)  $<1$ . Similar with the research of IMAYEV et al [16], the  $\beta$ -segregation was a result of rejection of Zr ( $\beta$ -stabilizer) into  $\beta/\alpha$  interphase boundaries during  $\beta \rightarrow \alpha$  transition. With increasing addition of Zr, the volume fraction of  $\beta_0$  phase was limited, while the volume fraction of  $\gamma$  phase increased vastly, which indicated that Zr preferred to diffusing into  $\gamma$  phase rather than remaining in  $\beta$  phase. KAINUMA et al [34] also indicated the partitioning coefficient  $k(\alpha/\gamma) < 1$ ,  $k(\alpha/\beta) < 1$  and  $k(\beta/\gamma) < 1$ .

The volume fractions of  $\gamma$  phase increased up to 3.09% with Zr addition of 5.0% in Ti43Al-xZr and 18.15% with Zr addition of 2.5% in Ti47Al-xZr. Both volume fractions of  $\gamma$  phase in Ti43Al-xZr and Ti47Al-xZr kept rising (Figs. 5 and 9), indicated that the addition of Zr promoted the formation of  $\gamma$  phase and thus the microstructure varied. The schematic diagram of increasing  $\gamma$  phase was illustrated in another paper. With appropriate addition of Zr, the microstructure was fine and homogenous, as shown in Sections 3.2 and 3.3, while severe micro-segregation occurred with excess addition of Zr, which was harmful to strength and ductility.

The solubilities of Zr in  $\gamma$  phase were 12.0% and 5.0% in Ti43Al-xZr and Ti47Al-xZr, respectively. However, the solubility of Zr in lamellar structure in Ti43Al was uncertain with a value higher than 4.0% and that in Ti47Al-xZr was about 1.3%. Obviously, large amount of Zr was dissolved into the matrix structure of lamellar colonies and  $\gamma$  phase, which would no doubt cause solution strengthening. Solution strengthening was an effective way in improving the strength and hardness, while the plasticity and toughness would decline to some extent.

The size of lamellar colonies gradually decreased with increasing addition of Zr in Ti43Al-xZr, and the smallest grain size (PDAS spacing) was 210.2  $\mu\text{m}$  with addition of 0.5% Zr in Ti47Al-xZr, which led to significant contribution to the strength enhancement by fine-grain strengthening. As discussed above, Zr was a stabilizer for  $\gamma$  and  $\beta$  phases. The addition of  $\beta$ -stabilizer would provide additional nucleation sites for  $\beta$  phase in the liquid and resulted in fine grains, which is similar to

the results in Ref. [35]. Fine-grain strengthening was beneficial to both the strength and ductility.

## 4.3 Mechanical performances

As mentioned in Section 2.4, the maximum compressive strength in Ti43Al-xZr was 1684.82 MPa with addition of 5.0% Zr, while the compressive strain fluctuated between 9.29% and 11.36%. The maximum compressive strength and compressive strain in Ti47Al-xZr were 2158.03 MPa and 35.24%, respectively, with addition of 0.5% Zr. The microstructure affected the mechanical properties.

The addition of Zr brought about effects of fine-grain strengthening and solution strengthening, and also resulted in micro-segregation. The combination of fine-grain strengthening and solution strengthening improved the compressive strength of Ti43Al-xZr and Ti47Al-xZr. For the fine-grain strengthening, the blocking force for dislocations significantly increased due to the increased number of grains and grain boundaries. Meanwhile, the plastic deformation could be extended into more grains to disperse the stress, which was beneficial to the ductility improvement. However, solution strengthening led to lattice distortion, blocking dislocation motion and causing slip deformation more difficultly, which was negative for ductility. Thus, the compressive strain in Ti43Al-xZr presented a fluctuated value with the combined effect of fine-grain strengthening and solution strengthening. With Zr addition more than 0.5% in Ti47Al-xZr, the inhomogeneous microstructure would lead to severe uncoordinated deformation and district stress concentration, which was markedly detrimental to compressive strength and compressive strain. In addition, the evenly dispersed basket weave of  $\beta$ -segregation in Ti43Al could hinder the migration of dislocations or grain boundaries, which was also beneficial to the compressive strength.

As shown in Fig. 12, both Ti43Al-xZr and Ti47Al-xZr presented transgranular fracture (splitting grains or colonies) and intergranular fracture (along the grains or colonies boundary). For the transgranular fracture, it was further divided into trans-lamellar fracture and inter-lamellar fracture. By comparison, the extension of trans-lamellar fracture needed more energy than inter-lamellar fracture, which was caused by stress concentration of inter-lamellar fracture. When meeting precipitate or boundary, the crack extension would convert from inter-lamellar into trans-lamellar under a certain degree of stress concentration, followed by inter-lamellar extension, then converted into trans-lamellar extension again. The above-mentioned promoted the formation of terrace-type morphology. In conclusion, with amounts of trans-lamellar fracture surfaces,

inter-lamellar fracture surfaces and river-markings, Ti43Al–xZr and Ti47Al–xZr alloys presented brittle fracture.

## 5 Conclusions

1) With addition of Zr, the microstructure morphology of Ti43Al–xZr hardly changed, showing equiaxed grains while that of Ti47Al–xZr was modified from dendrites into equiaxed grains. The microstructure was refined for both cases with grain size decreasing from 645.27 ( $x=0$ ) to 531.52  $\mu\text{m}$  ( $x=1.0\%$ ) in Ti43Al–xZr, and the primary dendrite arm spacing decreasing from 273.9 ( $x=0$ ) to 210.2  $\mu\text{m}$  ( $x=0.5\%$ ) in Ti47Al–xZr.

2) Zr was a strong  $\gamma$ -stabilizer showing the preference diffusion order of  $\gamma>\beta>\alpha$ , promoting the formation of  $\gamma$  phase vastly. Zr-rich  $\gamma$  phase mainly formed through  $\beta\rightarrow\gamma$  transition in Ti43Al–xZr and through  $\beta\rightarrow\alpha\rightarrow\gamma$  transition in Ti47Al–xZr. The solubilities of Zr in  $\gamma$  phase were 12.0% and 5.0% in Ti43Al and Ti47Al, respectively.

3) The alloys showed brittle fracture. The compressive properties were influenced by fine-grain strengthening, solution strengthening and micro-segregation. The compressive strength increased from 927.21 ( $x=0$ ) to 1684.82 MPa ( $x=5.0\%$ ) in Ti43Al–xZr, while the compressive strain fluctuated without a rule. For Ti47Al–xZr, the maximum compressive strength and compressive strain were 2158.03 MPa and 35.24% with addition of 0.5% Zr, improved by 9.46% and 7.64%, respectively.

## References

- [1] FU Yu-dong, ZHU Xiao-shuo, LI Zi-feng, LENG Ke. Properties and microstructure of Ti6Al4V by deformation accelerated low temperature plasma nitriding [J]. Transactions of Nonferrous Metals Society of China, 2016, 26: 2609–2616.
- [2] KOTHARI K, RADHAKRISHNAN R, WERELEY N M. Advances in gamma titanium aluminides and their manufacturing techniques [J]. Progress in Aerospace Sciences, 2012, 55: 1–16.
- [3] CHEN Rui-run, DING Hong-sheng, YANG Jie-ren, HUANG Feng, SU Yan-qing, GUO Jing-jie, FU Heng-zhi. Temperature field calculation on cold crucible continuous melting and directional solidifying Ti50Al alloys [J]. Transactions of Nonferrous Metals Society of China, 2012, 22: 647–653.
- [4] APPEL H F, PAUL J D H, OEHRING M. Gamma titanium aluminide alloys: Science and technology [M]. Weinheim: Wiley-VCH, 2011: 125–463.
- [5] CLEMENS H, MAYER S. Design, processing, microstructure, properties, and applications of advanced intermetallic TiAl alloys [J]. Advanced Engineering Materials, 2013, 15: 191–215.
- [6] OEHRING M, STARK A, PAUL J D H, LIPPMANN T, PYCZAK F. Microstructural refinement of boron-containing  $\beta$ -solidifying  $\gamma$ -titanium aluminide alloys through heat treatments in the  $\beta$  phase field [J]. Intermetallics, 2013, 32: 12–20.
- [7] ZHANG Dan-yang, LI Hui-zhong, LIANG Xiao-peng, WEI Zhong-wei, LIU Yong. Microstructure characteristic for high temperature deformation of powder metallurgy Ti–47Al–2Cr–0.2Mo alloy [J]. Materials & Design, 2014, 59: 415–420.
- [8] KONG Fan-tao, XU Xing-chen, CHEN Yu-yong, ZHANG De-liang. Microstructure and mechanical properties of large size as-cast Ti–43Al–9V–0.2Y (at.%) alloy ingot from brim to centre [J]. Materials & Design, 2012, 33: 485–490.
- [9] CHEN Rui-run, DONG Shu-lin, GUO Jing-jie, DING Hong-sheng, SU Yan-qing, FU Heng-zhi. Microstructure evolution and mechanical properties of directionally-solidified TiAlNb alloy in different temperature gradients [J]. Journal of Alloys and Compounds, 2015, 648: 667–675.
- [10] HALL E L, HUANG S C. Microstructures of rapidly-solidified binary TiAl alloys [J]. Acta Metallurgica et Materialia, 1990, 38: 539–549.
- [11] JIANG Hui-ren, HIROHASHI M, LU Yun, IMANARI H. Effect of Nb on the high temperature oxidation of Ti–(0–50 at.%)Al [J]. Scripta Materialia, 2002, 46: 639–643.
- [12] STRYCHOR R, WILLIAMS J C, SOFFA W A. Phase transformations and modulated microstructures in Ti–Al–Nb alloys [J]. Metallurgical and Materials Transactions A, 1988, 19: 225–234.
- [13] TAKAHASHI T, MINAMINO Y. Ternary diffusion and thermodynamic interaction in the  $\beta$  solid solutions of Ti–Al–Fe alloys at 1423 K [J]. Journal of Alloys and Compounds, 2012, 545: 168–175.
- [14] SUN Fu-sheng, CAO Chun-xiao, YAN Ming-guo, KIM S E, TAILEE Y. Alloying mechanism of beta stabilizers in a TiAl alloy [J]. Metallurgical and Materials Transactions A, 2001, 32: 1573–1589.
- [15] LIU Bin, LIU Yong, QIU Cong-zhang, ZHOU Can-xu, LI Jian-bo, LI Hui-zhong, HE Yue-hui. Design of low-cost titanium aluminide intermetallics [J]. Journal of Alloys and Compounds, 2015, 640: 298–304.
- [16] IMAYEV R M, IMAYEV V M, OEHRING M, APPEL F. Alloy design concepts for refined gamma titanium aluminide based alloys [J]. Intermetallics, 2007, 15: 451–460.
- [17] KIM S W, HONG J K, NA Y S, YEOM J T, KIM S E. Development of TiAl alloys with excellent mechanical properties and oxidation resistance [J]. Materials & Design, 2014, 54: 814–819.
- [18] FAN G J, SONG X P, QUAN M X, HU Z Q. Mechanical alloying and thermal stability of A167Ti25M8 (M=Cr, Zr, Cu) [J]. Materials Science and Engineering A, 1997, 231: 111–116.
- [19] JIANG X J, ZHOU Y K, FENG Z H, XIA C Q, TAN C L, LIANG S X, ZHANG X Y, MA M Z, LIU R P. Influence of Zr content on  $\beta$ -phase stability in  $\alpha$ -type Ti–Al alloys [J]. Materials Science and Engineering A, 2015, 639: 407–411.
- [20] BELOV N A, ALABIN A N, MATVEEVA I A, ESKIN D G. Effect of Zr additions and annealing temperature on electrical conductivity and hardness of hot rolled Al sheets [J]. Transactions of Nonferrous Metals Society of China, 2015, 25: 2817–2826.
- [21] JAYAPRAKASH M, PING D H, YAMABE-MITARAI Y. Effect of Zr and Si addition on high temperature mechanical properties of near- $\alpha$  Ti–Al–Zr–Sn based alloys [J]. Materials Science and Engineering A, 2014, 612: 456–461.
- [22] LÜ X Y, GUO E J, ROMETSCH P, WANG L J. Effect of one-step and two-step homogenization treatments on distribution of Al<sub>3</sub>Zr dispersoids in commercial AA7150 aluminium alloy [J]. Transactions of Nonferrous Metals Society of China, 2012, 22: 2645–2651.
- [23] YANG F, XIAO F H, LIU S G, DONG S S, HUANG L H, CHEN Q, CAI G M, LIU H S, JIN Z P. Isothermal section of Al–Ti–Zr ternary system at 1273 K [J]. Journal of Alloys and Compounds, 2014, 585: 325–330.

- [24] LI Yong-ping, LI Zhi, LIU Yong-xiong, WANG Xin-ming, ZHAO Man-xiu, YIN Fu-cheng. Isothermal section of Al–Si–Ce ternary system at 1073 K [J]. Journal of Phase Equilibria and Diffusion, 2014, 35: 276–283.
- [25] LAPIN J, GABALCOVÁ Z. Solidification behaviour of TiAl-based alloys studied by directional solidification technique [J]. Intermetallics, 2011, 19: 797–804.
- [26] IMAYEV R M, IMAYEV V M, OEHRING M, APPEL F. Alloy design concepts for refined gamma titanium aluminide based alloys [J]. Intermetallics, 2007, 15: 451–460.
- [27] WITUSIEWICZ V T, BONDAR A A, HECHT U, REX S, VELIKANOVA T Y. The Al–B–Nb–Ti system: III. Thermodynamic re-evaluation of the constituent binary system Al–Ti [J]. Journal of Alloys and Compounds, 2008, 465: 64–77.
- [28] WANG Qiang, DING Hong-sheng, ZHANG Hai-long, LIU Shi-qiu, CHEN Rui-run, GUO Jing-jie, FU Heng-zhi. Microstructure and compressive properties of directionally solidified Er-bearing TiAl alloy using cold crucible [J]. Materials & Design, 2016, 99: 10–20.
- [29] TAKEYAMA M, KOBAYASHI S. Physical metallurgy for wrought gamma titanium aluminides: Microstructure control through phase transformations [J]. Intermetallics, 2005, 13: 993–999.
- [30] CHENG T T. The mechanism of grain refinement in TiAl alloys by boron addition—An alternative hypothesis [J]. Intermetallics, 2000, 8: 29–37.
- [31] CHENG T T, LORETTO M H. The decomposition of the beta phase in Ti–44Al–8Nb and Ti–44Al–4Nb–4Zr–0.2Si alloys [J]. Acta Materialia, 1998, 46: 4801–4819.
- [32] TETSUI T, SHINDO K, KOBAYASHI S, TAKEYAMA M. A newly developed hot worked TiAl alloy for blades and structural components [J]. Scripta Materialia, 2002, 47: 399–403.
- [33] HU D, JIANG H, WU X. Microstructure and tensile properties of cast Ti–44Al–4Nb–4Hf–0.1Si–0.1B alloy with refined lamellar microstructures [J]. Intermetallics, 2009, 17: 744–748.
- [34] KAINUMA R, FUJITA Y, MITSUI H, OHNUMA I, ISHIDA K. Phase equilibria among  $\alpha$  (hcp),  $\beta$  (bcc) and  $\gamma$  ( $L1_0$ ) phases in Ti–Al base ternary alloys [J]. Intermetallics, 2000, 8: 855–867.
- [35] JIN Y G, WANG J N, YANG J, WANG Y. Microstructure refinement of cast TiAl alloys by  $\beta$  solidification [J]. Scripta Materialia, 2004, 51: 113–117.

## Zr 对二元钛铝合金组织和力学性能的影响

陈瑞润, 赵晓叶, 杨勇, 郭景杰, 丁宏升, 苏彦庆, 傅恒志

哈尔滨工业大学 材料科学与工程学院, 哈尔滨 150001

**摘要:** 采用非自耗真空电弧熔炼炉制备不同 Zr 含量的 Ti43Al 与 Ti47Al 合金, 研究该合金的显微组织和力学性能的变化。结果表明: Zr 对 Ti43Al 合金的组织形态无明显影响, Ti47Al 合金则由枝晶组织演变成等轴晶组织。Zr 元素的添加能细化晶粒。Zr 能促进  $\gamma$  相的形成, Zr 在 Ti43Al 和 Ti47Al 合金  $\gamma$  相中的固溶度分别为 12.0% 和 5.0% (摩尔分数)。经过分析, Ti43Al–xZr 中的  $\gamma$  相由  $\beta$  相转化而来, Ti47Al–xZr 中的  $\gamma$  相则由  $\alpha$  相转化而来。细晶强化和固溶强化作用使压缩强度提高; 然而, 严重的显微偏析会导致力学性能下降。Zr 元素极大的固溶度对合金的塑性具有不利的影响。Ti43Al–xZr 和 Ti47Al–xZr 合金的最大压缩强度分别为 1684.82 MPa ( $x=5.0\%$ ) 和 2158.03 MPa ( $x=0.5\%$ ), 而 Ti43Al–xZr 合金的压缩应变无明显变化, Ti47Al–xZr 合金的最大压缩率为 35.24% ( $x=0.5\%$ )。两组合金均呈脆性断裂特征。

**关键词:** TiAl 二元合金; Zr; 显微组织演变; 相转变; 压缩性能

(Edited by Wei-ping CHEN)